Journal of Ovonic Research Vol. 14, Nr. 4, July – August 2018, p. 307 - 316

STUDYING THE MECHANICAL PROPERTIES OF BARIUM STRONTIUM TITANATE CERAMICS BY AN ULTRASONIC PLUSE ECHO TECHNIQUE

H. ABOMOSTAFA*, M. ELLAMEY
Physics Department, Faculty of Science, Menoufia University, Shebin El-Koom, Egypt

$Ba_{1-x}Sr_xTiO_3$ ($0 \leq x \leq 0.5$) ceramics were prepared by solid state reaction. X- ray diffraction pattern and FMSEM micrographs showed the compositions of these ceramics are single tetragonal phase except for $Ba_{0.5}Sr_{0.5}TiO_3$ showed single cubic phase. The crystal size and the lattice parameters decreased as Sr content increases and confirm the formation of single phase. Mechanical properties were studied by an ultrasonic pulse echo technique at 2 MHz. Increasing of Sr content led to remarkable increase in all elastic moduli. The values of longitudinal modulus (L), shear modulus (G), Young's modulus (E), and bulk modulus (B) increased from 9.15 to 20.64 GPa, 3.29 to 7.43 GPa, 8.02 to 18.11 GPa, and 4.76 to 10.73 GPa, respectively. High temperature ultrasonic studies showed that the Curie transition temperature depends on the content of Sr in the compositions, where to shift from 353.7 to 290 °C with increasing Sr content. Also, the appeared two relaxation peaks and its origin were investigated.

(Received June 6, 2018; Accepted August 16, 2018)

Keywords: BST ceramics, Phase transition, Mechanical properties, Ultrasonic attenuation

1. Introduction

Barium titanate ($BaTiO_3$) is a ferroelectric material known for its high dielectric constant, low dissipation factor and positive temperature coefficient [1–3]. Strontium titanate ($SrTiO_3$) is an incipient ferroelectric i.e., it exhibits quantum ferroelectricity, which implies that though it undergoes phase transition at very low temperatures (*Tc* = 105 K), the quantum effect prevents complete transition to paraelectric phase. Therefore, $SrTiO_3$ exhibits both ferroelectric and paraelectric behaviors, i.e., it is ferroelectric below its Curie temperature and paraelectric beyond it [4]. When $SrTiO_3$ is added to $BaTiO_3$ to form a solid solution, Ba ions can be replaced by Sr ions lead to form the prevskite structure $Ba_{(1-x)}Sr_{(x)}TiO_3$ or BST. The Curie temperature of BST depends on the amount of Sr in the (Ba, Sr)TiO_3 lattice, it decreases linearly with increasing Sr. The ferroelectric / paraelectric transition temperature enables the BST materials to be tailored for specific applications by varying Sr content. Therefore, depending on Ba: Sr ratio, transition temperature and, hence, electrical and optical properties of the BST demonstrate a variation over a broad range [5, 6]. Barium strontium titanate has considerably attracted interest of researchers and engineers due to high dielectric permittivity, low optical losses, ferroelectric activity and composition dependent Curie temperature [7]. Because of its perovskite structure , BST has been used as a high voltage capacitor, tunable filter, detector, piezoelectric, sensor, pressure transducer, actuator, optoelectronic device and so on [8, 9]. BST have been synthesized by the solid state reaction [10], polymeric precursor [11], sputtering [12], pulsed laser deposition (PLD) [13, 14], metal-organic chemical vapor deposition (MOCVD) [15], hydrothermal [16, 17] and sol–gel methods [18–20]. Mechanical properties investigations are not too much and restricted to some published work on BST ceramics where carried out at low frequencies (a few Hz and kHz) [21-25] with an inverted pendulum and little work has been performed in the MHz range [10, 11]. Those works dealt with mechanical losses (internal frictions) and shear moduli, attenuation and velocity of waves.

*Corresponding author: halaabomostafa@yahoo.com

This work aims to: Preparation of $Ba_{1-x}Sr_xTiO_3$ ceramic materials with different Sr where ($0 \leq x \leq 0.5$): Characterizing the structure of prepared BST materials by x- ray diffraction, FESEM, and EDX; Investigating the mechanical properties such as velocities of ultrasonic wave, elastic moduli, attenuation, at room temperature as well as the dependence of both the structural phase transition (the Curie point T_c) and the relaxation phenomena on temperature in tested ceramics.

2. Experimental procedures

BST ceramics with the chemical formula $Ba_{1-x}Sr_xTiO_3$, ($0 \leq x \leq 0.5$) were prepared by the conventional solid state method. Reagent-grade $BaCO_3$, $SrCO_3$, and TiO_2 were mixed in the appropriate molar ratios and ground thoroughly by an agate vibratory micro mill for 6 h. The mixtures were calcined at 1150°C for 8 h in open air. The obtained calcined compositions were ground for another 4h. The produced fine powders were pressed into disc-shaped pellets (10 mm in diameter and 0.6–1.5 mm in thickness) at an isostatic pressure of 12 ton. The pelletized samples were sintered at 1250°C for 3 h. The obtained sintered compositions were ground for another 4h. The produced fine powders were pressed into disc-shaped pellets (10 mm in diameter and 0.6–1.5 mm in thickness) at an isostatic pressure of 12 ton. The pelletized samples were finally sintered at 1100°C for 8 h. The structure of samples were characterized by X-ray diffraction using analytical X'Pert PRO MRD diffract meter system having CuKα (λ =1.540598 Å) with 2θ range, 5 - 80°. The obtained XRD data was utilized to calculate the crystallite size using the following Scherer equation [26, 27]:

$$D = \frac{0.9\,\lambda}{\beta\, cos\theta} \tag{1}$$

Field emission scanning electron microscope (FESEM) Quanta FEG 250 was used to analyze the samples topography.

The density of ceramics was measured by an Archimedean method. The Archimedean determined bulk density ρ_{exp} and the theoretically density ρ_{th} from the XRD data of tested samples were used to calculate the percentage porosity based on the equation [28]:

$$\text{Porosity \%} = (\rho_{th} - \rho_{exp}) / \rho_{th} \tag{2}$$

The ultrasonic wave velocities v(in ms^{-1}) propagated in the samples and attenuation α (dB/cm) were measured at room temperature, using pulse-echo technique MATEC Model MBS8000 DSP (ultrasonic digital signal processing) system with 2 MHz resonating. Silicon grease was used as bonding material between X-cut and Y-cut transducers and tested samples. The ultrasonic wave velocities v were calculated by taking the elapsed time between the initiation and the receipt of the pulse appearing on the screen. It can be calculated using the following equation

$$v = \frac{2x}{\Delta t} \tag{3}$$

where x is the sample thickness and Δt is the time interval. The measurements were repeated three times to check the reproducibility of the data. The estimated accuracy of the velocity measurement is about 0.04%. The values of elastic moduli; namely longitudinal modulus (L), shear modulus (G), Young's modulus (E), bulk modulus (B) and Poisson's ratio (σ) were obtained from the longitudinal $(V_L)^2$ and shear $(V_S)^2$ ultrasonic velocities and calculated from the following equations:

$$L = \rho v_L^2 \tag{4}$$

$$G = \rho\, v_s^2 \tag{5}$$

$$E = \frac{G(3L-4G)}{(L-G)} \tag{6}$$

$$B = L - \frac{4}{3}G \tag{7}$$

To measure ultrasonic attenuation α, the heights of some successive echoes were used according to this equation [29]

$$\alpha = \frac{-20log\left({}^{A_m}/_{A_n}\right)}{2(m-n)x} \tag{8}$$

where A_m and A_n are the amplitudes of the mth and nth echoes and x is the specimen thickness. The calculated values of α were accurate to 0.1% dB/mm.

3. Results and discussion

Fig. 1a shows the XRD patterns of $Ba_{1-x}Sr_xTiO_3$ ($0 \leq x \leq 0.5$). This figure reveals all XRD peaks as recorded for each tested sample which confirm the formation of a single phase, perovskite BST structure.

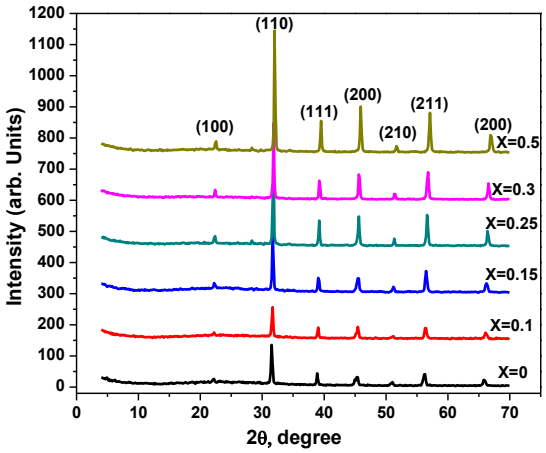

Fig. 1 (a). XRD patterns of $Ba_{1-x}Sr_xTiO_3$ ($0 \leq x \leq 0.5$) ceramics

All peaks are indexed as shown in Fig. 1a, relating to its reflections of various polycrystalline orientations [21, 30, 31] as indicated with (110) index as the high intensity major peak. Also, inspection of peaks positions in the above figure, it is observed that, as the Sr content increases the diffraction peaks shift towards higher angles side suggesting a progressive reduction in lattice parameters, which can be established due to the substitution of the smaller Sr^{2+} ions for the larger Ba^{2+}. This also confirms that Sr^{2+} ions have involved the site of Ba^{2+} rather than Ti^{4+} whose ionic radius (0.61A˚) which is significantly smaller as compared with those of Sr^{2+} (1.44A˚) and Ba^{2+} (1.61A˚) [21]. However, this was verified by doing a closer observation of (110) peaks for all samples as illustrated in Figure 1b where the peak position is appeared at 2θ° angles: 31.5779°, 31.68623°, 31.75117°, 31.83251°, 31.88799°, and 32.06737° with increasing Sr content from 0 to 0.5 % mole fraction, respectively.

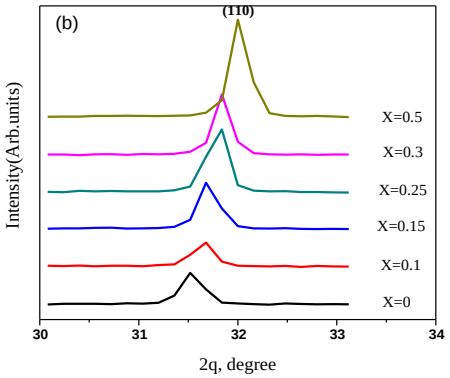

Fig. 1(b). XRD peaks of (110) plane for $Ba_{1-x}Sr_xTiO_3$ ($0 \leq x \leq 0.5$) ceramics

The crystallite size $D_{(hkl)}$ is estimated in terms of x-ray line half width broadening using Scherrer's equation. The evolution of crystal structure, lattice parameters and crystallite size obtained from XRD data are listed in table 1. Table 1 shows with increasing the Sr content lead to decreasing both of lattice parameters and crystallite size. The crystal structure showed tetragonal phases for all tested samples except for at x = 0.5 showed cubic phase. The Tetragonal-ity ratio (c/a) decreased as Sr content increased as reported [32].

Table 1. Lattice parameters, a, c, Crystal structure, the ratio (c/a), Volume of unit cell and Crystallite Size D of tested $Ba_{1-x}Sr_xTiO_3$

x Sr content	Lattice parameter a (Å)	Lattice parameter c (Å)	Crystal structure	The Tetragonal-ity ratio (c/a)	Volume of unit cell $V(Å)^3$	Crystallite size D (nm)
0	3.99597	4.0124	Tetragonal	1.0041	64.069	27.5
0.1	3.9829	4.00679	Tetragonal	1.0061	63.5617	26.7
0.15	3.9785	3.9938	Tetragonal	1.0038	63.216	20.6
0.25	3.9771	3.9883	Tetragonal	1.00294	63.08	19.7
0.3	3.9626	3.9733	Tetragonal	1.0027	62.39	18.3
0.5	3.9471	3.9471	Cubic	1.0000	61.49	16.5

The $Ba_{1-x}Sr_xTiO_3$ ($0 \leq x \leq 0.5$) samples have been investigated by (FESEM). Fig. 2 shows that, the surface of the prepared samples indicate the appearance of grains which are uniformly distributed and the grain size decreases and the porosity increases with increasing the concentration of (Sr). Also, the distribution and the homogeneity of grains suggest that the formation of the single-phase with grains look like of spherical shape.

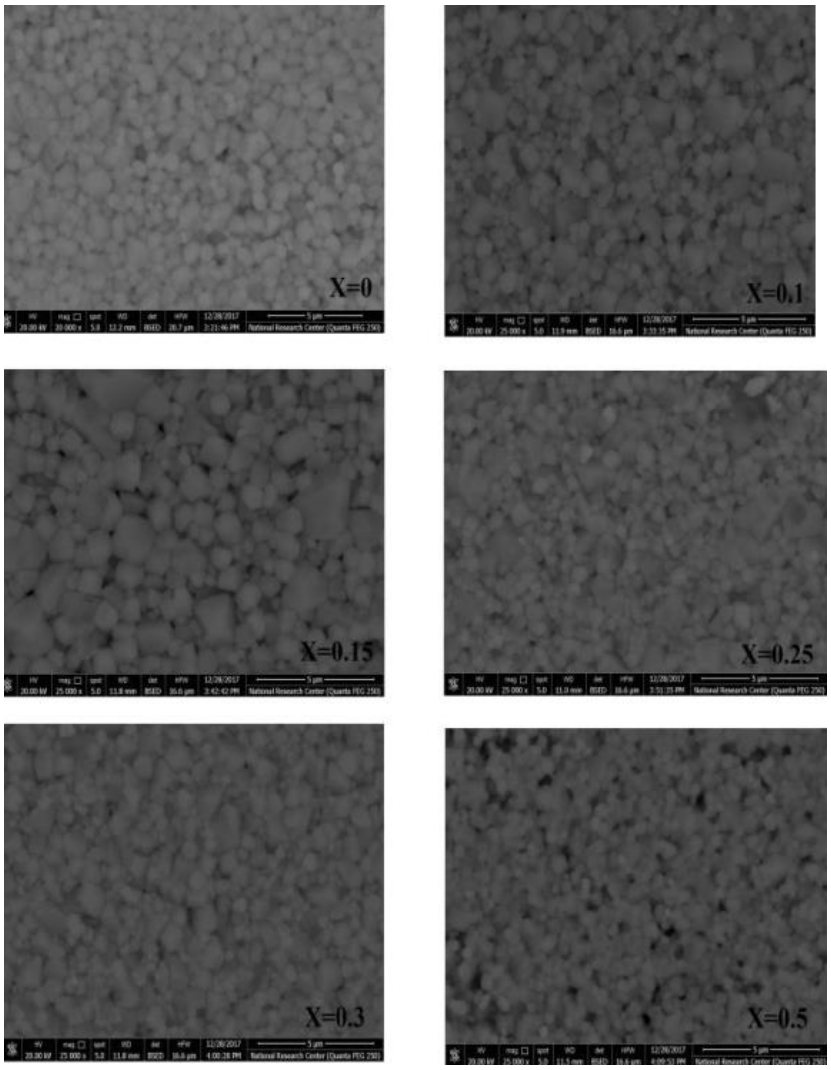

Fig. 2 (a-f). FESEM micrograph of the surface of $Ba_{1-x}Sr_xTiO_3$ ($0 \leq x \leq 0.5$) ceramics

Fig. 3 shows EDAX area and point analyses for obtained microstructure of the tested samples. Inspection of this figure reveals that, the different concentrations of (Ba, Sr, O and Ti) employed elements in the tested BST ceramics material are obviously indicated by the peaks originated from these elements.

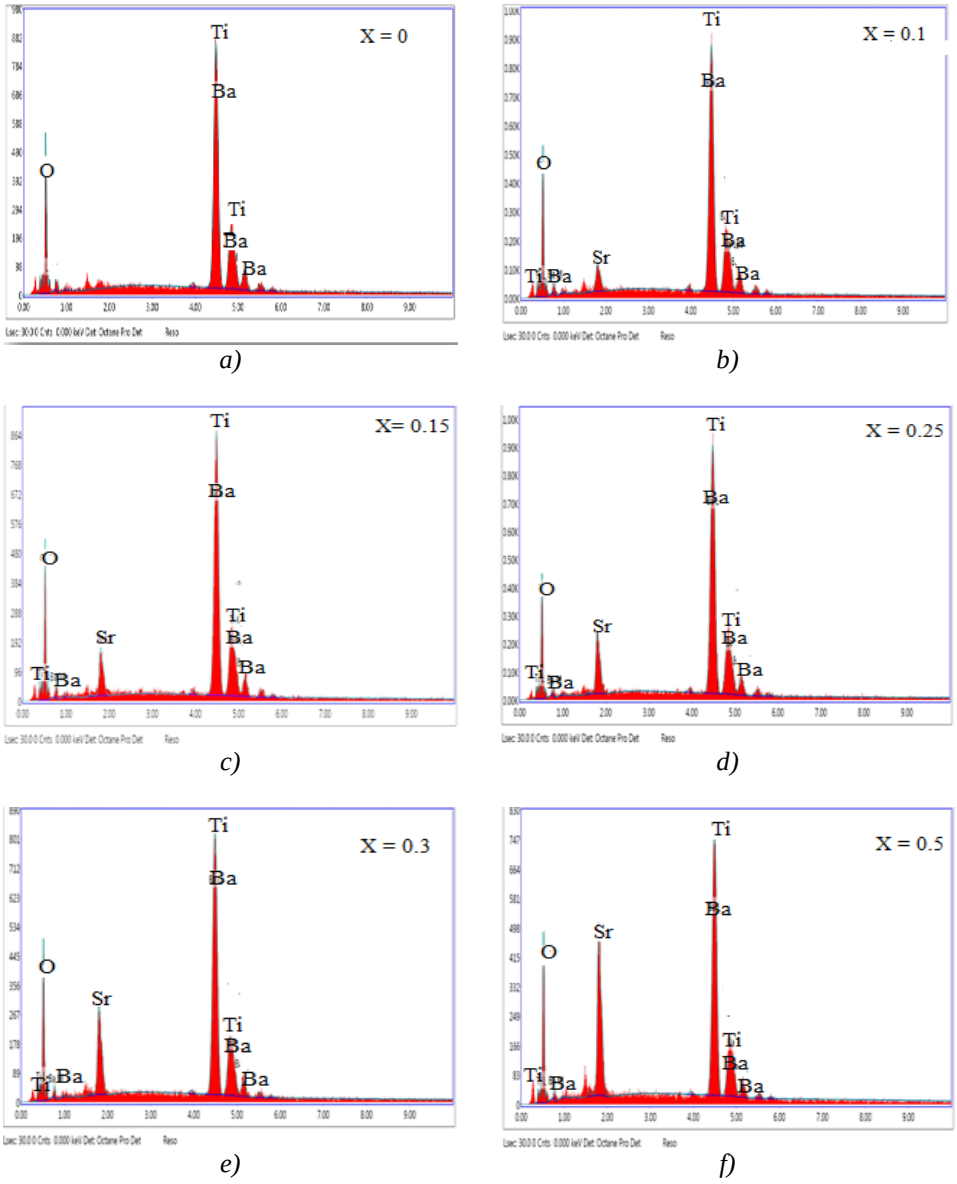

Fig. 3 (a-f). EDAS area analysis of $Ba_{1-x}Sr_xTiO_3$ ($0 \leq x \leq 0.5$) ceramics

The elements ratios are near and matched to the above chemical stoichiometric values of x and they are listed in Table 2.

Table 2. The values of elements composition by EDS

Composition	Br content	Sr content	Ti content	O content
$BaTiO_3$	38.04	0	18.5	43.45
$Ba_{0.9}Sr_{0.1}TiO_3$	32.31	5.53	18.78	43.39
$Ba_{0.85}Sr_{0.15}TiO_3$	31.99	7.63	18.05	42.33
$Ba_{0.75}Sr_{0.25}TiO_3$	30.15	10.78	19.63	39.44
$Ba_{0.7}Sr_{0.3}TiO_3$	19.58	17.5	18.06	44.86
$Ba_{0.5}Sr_{0.5}TiO_3$	19.15	17.39	18.67	44.79

Fig. 4 shows the compositional dependences of both the bulk density and porosity% of tested BST ceramics. It reveals that the bulk density decreases from 5194 to 4680 kg/m^3 as the Sr

content increases from 0 to 0.5 mole fraction. While the apparent porosity presented exhibits an opposite trend for that of bulk density. It increased from 14.06 to 16.82 %. The observed decrease in the bulk density is attributed to the increase in the porosity that established from the fact that the atomic weight of Sr^{2+} (87.62) is lower than that of Ba^{2+} (137.3). This is in agreement with the previous results [33, 35].

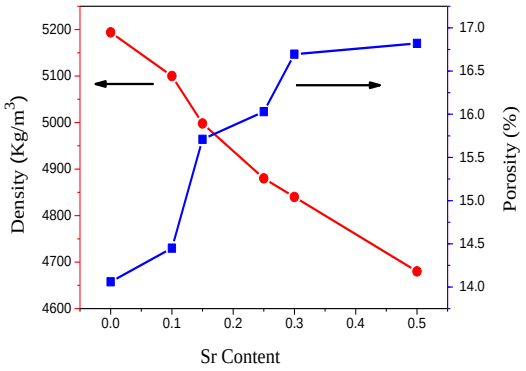

Fig. 4. Bulk density and porosity % of $Ba_{1-x}Sr_xTiO_3$ ($0 \leq x \leq 0.5$) ceramics

Fig. 5 shows the longitudinal modulus (L), shear modulus (G), Young's modulus (E), and bulk modulus (B) increased from 9.15 to 20.64 GPa, 3.29 to 7.43 GPa, 8.02 to 18.11 GPa, and 4.76 to 10.73 GPa, respectively.

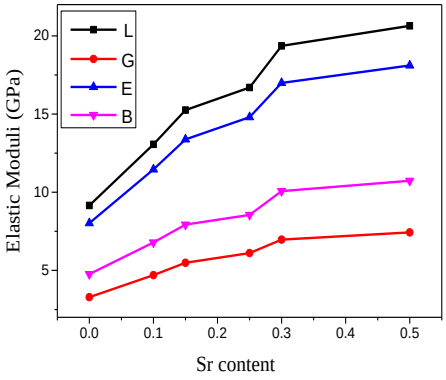

Fig. 5. Variations of Young's modulus (E), longitudinal modulus (L), bulk modulus (B), and shear modulus (G) with Sr content

The increment of the elastic moduli may be due to decrease of both the crystallite size and Tetragonal-ity ratio as discussed by x- ray diffraction and the increasing the porosity as the Sr content increases in the samples. The reported data of the elastic moduli was comparable with those reported previously [36].

The attenuation of ultrasonic waves α in (dB/cm) at 2 MHz was studied at room temperature and at temperature variations. Fig. 6 showed attenuation of ultrasonic waves at room temperature decreased as the Sr content increased in the sample. This behavior refers to the increasing formation of pores, the decreasing in grain and particles sizes as the Sr content in the samples increases, as seen by XRD in the present formed perovskite polycrystalline structure in agreement with previous results [10, 31, 32, 33, 37].

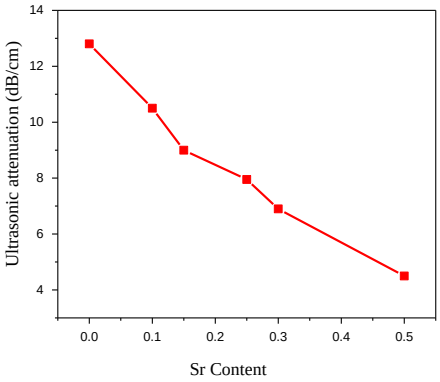

Fig. 6. The variation of ultrasonic attenuation with Sr content at room temperature

Attenuation of the ultrasonic waves, α was studied during temperature variation at 2 MHz frequency for prepared $Ba_{1-x}Sr_xTiO_3$ samples with x = 0, 1, 0.15 and 0.25 Sr content and the obtained spectra are shown in Fig. 7(a - d). The plot corresponding to each sample in these figures shows a high temperature of large intensity attenuation peak which indicates the Curie temperature (or the structural phase transition ferroelectric tetragonal into a para-electric cubic one with increasing temperature) of these materials [22, 30]. It is also observed in Fig. 7(a - d) that the increase of the Sr content in the ceramic materials decrease the Curie temperature from 353.7 to 290 °C as seen in table 3 and the attenuation peaks are broadened. Besides, two small damping peaks are appeared and located at lower temperatures below the Curie transition temperature, and named as relaxation peaks [21, 22, 30]. It is worth mentioning that all the curves start at room temperature measurements and showing shoulders indicating the right wings of the orthorhombic to tetragonal structural ferroelectric phase transition which seems to occur around 0°C temperature [10, 23, 25, 33].

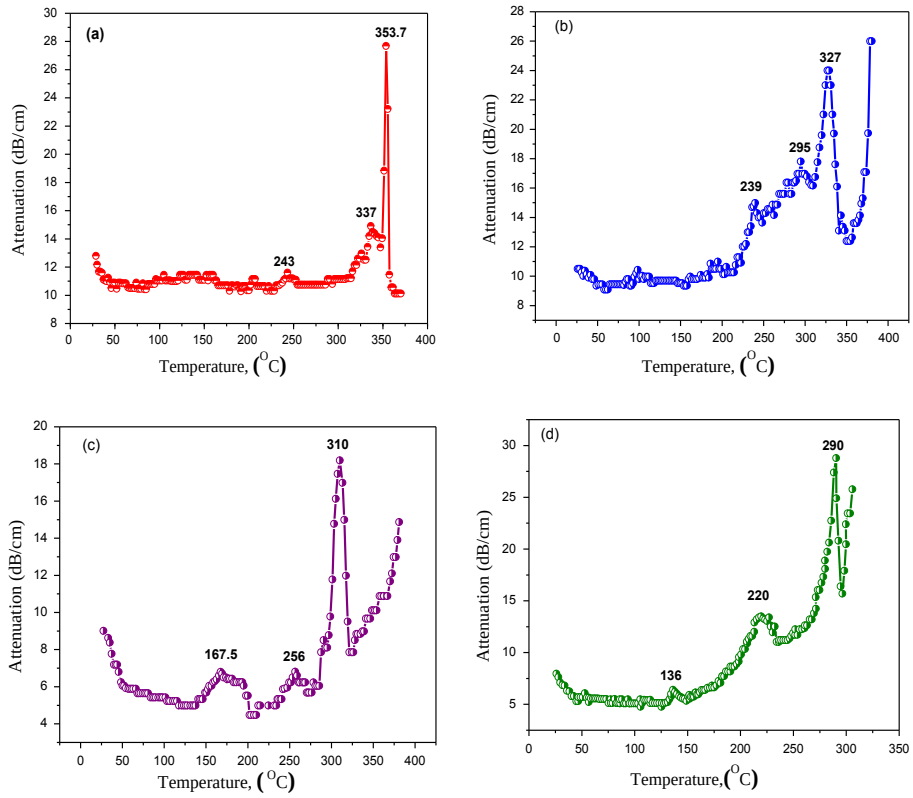

Fig. 7. The variation of ultrasonic attenuation with temperature $B_{1-x}Sr_x\ TiO_3$ ceramics: (a) x = 0 , (b) x =0.1 , (c) x =0.15 and (d) x =0.25 , respectively

The positions of Curie transition and relaxation peaks temperature which observed for all samples are listed in table 3. The Curie transition and relaxation peaks temperature shifted to lower temperature as Sr content increase. The occurrence of these peaks in this range of temperatures may be due to the high operated frequency at 2 MHz while other works were carried out at low frequencies (several Hz) [23, 25]. The relaxation peaks were discussed according to the calculated values of its activation energy. Where to the relaxation peaks of activation energy smaller than 1.1 eV could be interpreted to diffusion of oxygen vacancies associated with domain walls and for relaxation peaks with energies larger than 1.1 eV were attributed to diffusion of point defects in ferroelectric phase of these ceramics [22, 30]. Considering the previous results and applying the Arrhenius relaxation equation [30], the activation energies for both phase structural and relaxation peaks are calculated and listed in Table 3.

Table 3. The values of Curie temperature, first and second relaxation peak temperatures and their activation energies

Sr content	Curie Temperature (°C)	First Relaxation Peak Temp (°C)	Second Relaxation Peak Temp. (°C)	Activation Energy of first peak (eV)	Activation Energy of second peak (eV)
0	353.7	337	243	1.38	1.81
0.1	327	294	239	1.7	2.05
0.15	310	256	167	1.86	2.16
0.25	290	220	136	2.2	2.41

On the other hand, the calculated values for the first and second activation energy due to first and second relaxation peaks increased from 1.38 to 2.2 eV and 1.81 to 2.41 eV respectively. This activation energy values are greater than 1.1 eV and interpreted to diffusion of point defects in the ferroelectric phase of the tested ceramic materials.

4. Conclusions

$Ba_{1-x}Sr_xTiO_3$, ($0 \leq x \leq 0.5$) ceramics were prepared by solid state reaction technique. XRD data confirmed the formation of single phase perovskite structures where to the composition with Sr content ≤ 0.4 mole fraction showed tetragonal phase and for Sr content = 0.5 mole fraction showed cubic phase. FMSEM showed that the grain size decreased as the Sr content increased also confirm the formation of single phase.

The density of the samples decreased while the porosity increased with increasing the Sr content. Increasing of Sr content led to remarkable increase in all elastic moduli and decrease in ultrasonic attenuation. Increasing of Sr content shifts the Curie transition temperature toward lower temperature. Also, the two relaxation peaks and its origin were investigated.

References

[1] H. L. Gong, X. H. Wang, S. P. Zhang, L. T. Li, Mater. Res. Bull. **73**, 233 (2016).
[2] D. Xu, W. L. Li, L. D. Wang et al., Acta. Mater. **79**, 84 (2014).
[3] V. Paunovic, V. V. Mitic, L. Kocic, J. Ceram. Int. **42**, 11692 (2016).
[4] K. Morito, Y. Iwazaki, T .Suzuki, M .Fujimoto, J Appl. Phys. **94**, 5199 (2003).
[5] S. Lahiry, Mansingh, Thin Solid Films **516**, 1656 (2008).
[6] M. R. Mohammadi, D. J. Fray Particuology **9**, 235 (2011).
[7] H. Kobayashi, T. Kobayashi, Jpn. J. Appl. Phys. **33**m L533 (1994).
[8] Y. Gao, V. V. Shvartsman, D. Gautam, M. Winterer, D. C. Lupascu, J. Am. Ceram. Soc. **97**, 1 (2014).

[9] S. M. Olhero, A. Kaushal, J. M. F. Ferreira, J. Am. Ceram. Soc. **97**, 725 (2014).
[10] M. H. Badr, L. M. Sharaf El-Deen, A. H. Khafagy, D. U. Nassar, J. Electroceram**. 27**, 189 (2011)
[11] L. Zhou, P. M. Vilarinko, J. L. Baptista, J. Eur. Ceram. Soc. **21**. 531 (2001).
[12] Z. Xu, D. Yan, D. Xiao, P. Yu, J. Zhu, Ceram. Int. **39**. 1639 (2013).
[13] V. V. Buniatyan, M. H. Abouzar, N. W. Martirosyan, J. Schubert, S. Gevorgian, M. J. Schoning et al., Phys. Status Solidi A **207**, 824 (2010).
[14] K. C. Sekhar, S. H. Key, K. P. Hong, C. S. Han, J. M. Yook, D. S. Kim et al., Curr. Appl. Phys.**12**, 654 (2012).
[15] C. S. Kang, C. S. Hwang, H.-Ju. Cho, B. T. Lee, S. O. Park, J. W. Kim, H. Horii et al., Jpn. J. Appl. Phys. **35**, 4890 (1996) .
[16] Z. Zhou, H. Tang, Y. Lin, H. A. Sodano, Nanoscale **5**, 10901 (2013).
[17] J. Cirkovica, K. Vojisavljevica, N. Nikolica, P. Vulicc, Z. Brankovica, T. Sreckovica et al., Ceram Int. **41**, 11306 (2015).
[18] S. H. Xiao, W. F. Jiang, K. Luo, J. H. Xia, L. Zhang, Mater. Chem. Phys. **127**, 420 (2011).
[19] B. Li, C. Wang, W. Liu, Y. Zhong, R. An, Mater Lett. **75**, 207 (2012).
[20] D. Sette, V. Kovacova, E. Defay, Thin Solid Films **589**, 111 (2015).
[21] C. Fu, C. Yang, H. Chan, Y. Wang, L. Hu, Mater. Sci. Eng. B **119**, 185 (2005).
[22] B. L. Cheng, M. Gabbay, G. Fantozzi, W. Jr. Duffy, J. Alloy. Comp. **211**, 352 (1994).
[23] B. L. Cheng, M .Gabbay, M. Maglione, G. Fantozzi, J. Electroceram. **10**, 5 (2003).
[24] H. V. Alexandru, C. Berbecaru, A. Ioachim, Mater. Sci. Eng. B **109**, 152 *(*2004).
[25] H. Frayssignes, B. L. Cheng, G. Fantozzi, T.W. Button, J. Eur. Ceram. Soc. **25**, 3203 (2005).
[26] R. A. Youness, M. A. Taha, M. Ibrahim, Mol. Struct. **1150**, 188 (2017).
[27] R .A. Youness, M. A. Taha, H. Elhaes, M. Ibrahim, Comput. Theor. Nanos. **14**(5), 2409 (2017),
[28] O. P. Thakur, Chandra, D. K. Agrawal Materials Science and Engineering B **96**, 221 (2002).
[29] V. Rajendran, J. Non-Cryst. Solids **77**, 353 (2007).
[30] Y. C. Liou, C. T. Wu, Cerm. Int. **34** ,517 (2008).
[31] A. K. Singh, R. N. Barik, P. Choudhary, P. K. Mahapatara, J. Alloy Compd. **479**, 39 (2009).
[32] Yun Sining, Wang Xiaoli, Bo Li, Xu Delong, Solid State Communications **143**, 461 (2007).
[33] L. M.. Sharaf El-Deen, M. H. Badr, Abdel-Mageed H. Khafagy, Dalia U. Nassar Crystal Structure Theory and Applications **2**, 132 (2013).
[34] A. Ioachim, M. I. Toaxan, M. G. Banclu, L. Nedelcu, A. Dutu, S. Antohe, C. Berbecaru, L. Georescu, G. Stoica, H.V. Alexandru, Thin Solid Films **515**, 6289 (2007).
[35] C. Berbecaru, H. V. Alexandru, C. Porosnicu, A. Vele, A. Ioachim, L. Nedelcu, M. Toascan, Thin Solid Films **516**, 8210 (2008).
[36] Te Hua Fang, Jin Chang Win, Ming Lin Chao, Wen Ji Liang, Shin Changd Yee, Jen Hsiao Yu Materials Science and Engineering A **426**, 157 (2006).
[37] S. Kongtaweelert, D. C. Siclair, S. Panichphant, Curr. Appl. Phys. **6**, 474 (2006).